Heat and fluid flow in complex joints during gas metal arc welding—Part I: Numerical model of fillet welding

W. Zhang, C.-H. Kim, and T. DebRoy[a)]
Department of Materials Science and Engineering, The Pennsylvania State University, University Park, Pennsylvania 16802

(Received 11 November 2003; accepted 4 February 2004)

Gas metal arc (GMA) fillet welding is one of the most important processes for metal joining because of its high productivity and amiability to automation. This welding process is characterized by the complicated V-shaped joint geometry, a deformable weld pool surface, and the additions of hot metal droplets. In the present work, a three-dimensional numerical heat transfer and fluid flow model was developed to examine the temperature profiles, velocity fields, weld pool shape and size, and the nature of the solidified weld bead geometry during GMA fillet welding. The model solved the equations of conservation of mass, momentum, and energy using a boundary fitted curvilinear coordinate system. Apart from the direct transport of heat from the welding arc, additional heat from the metal droplets was modeled considering a volumetric heat source. The deformation of the weld pool surface was calculated by minimizing the total surface energy. Part I of this article is focused on the details of the numerical model such as coordinate transformation and calculation of volumetric heat source and free surface profile. An application of the model to GMA fillet welding of mild steel is described in an accompanying article (W. Zhang, C.-H. Kim and T. DebRoy, J. Appl Phys. **95**, 5220 (2004)). [DOI: 10.1063/1.1699485]

I. INTRODUCTION

During arc fusion welding, the structure and properties of welds are influenced by the simultaneous occurrence of several important physical processes. These include the absorption of arc energy, formation of the weld pool, vigorous circulation of the molten material in the pool, heat transfer in the entire weldment, and the solidification of the molten material.[1–3] Much of the contemporary research work on these component processes was motivated by the appreciation that the improved understanding would ultimately lead to better welds. Because of the small size of the weld pool, the presence of plasma in its vicinity, very high temperatures, and the sharp temperature gradients in a fairly small region, physical measurements of important parameters such as temperature and velocity fields are very difficult tasks. Therefore, mathematical modeling is a practical recourse and provides fundamental and quantitative understanding of various weldment characteristics. Examples include quantitative understanding of weld temperature and velocity fields,[4–7] phase composition,[8,9] grain structure,[10,11] inclusion structure,[12] and evaporation of alloying elements.[13]

Previous computer simulation efforts to understand welding processes and welded materials through numerical heat transfer and fluid flow calculations have focused mainly on simple systems. Most of the studies considered rectangular workpiece and ignored any deformation of the weld pool top surface (flat top surface). These models worked well for gas tungsten arc or laser conduction mode welding of butt welds for a wide variety of welding conditions in materials with diverse thermophysical properties.[4–13] However, such simple models are not readily applicable to widely used gas metal arc (GMA) fillet welding process because of the complexities in the weld geometry and welding process. During GMA fillet welding, superheated liquid metal droplets formed from the consumable electrode carry heat and mass into the weld pool. Depending on the current and the voltage, the arc can exert significant pressure on the pool top surface. The deformation of the weld pool surface can affect heat transfer and fluid flow and the eventual solidified surface profile of the weld bead. The complexity of the welding process is further augmented by the complicated V-shaped fillet joint geometry containing curved weld pool surface. All these complexities must be taken into account to accurately model GMA fillet welding processes.

A fundamental understanding of heat transfer and fluid flow considering free surface deformation is still evolving. Although significant progresses have been made in the modeling of GMA welding of butt joints with free surface deformation,[14–17] a three-dimensional framework for understanding of heat transfer and fluid flow based on scientific principles still remains to be undertaken for GMA welding of fillet joints due to its complexity. With the advancement of computational hardware and software, it has now become practical to relax some of the simplifying assumptions of the previous research and address more realistic situations.

In the present work, a three-dimensional numerical model was developed to investigate the heat transfer, fluid flow, and the solidified surface profile during GMA fillet welding. The model used a boundary fitted coordinate system to accurately calculate temperature and velocity fields in the complex V-shaped physical domain containing a deformable weld pool surface. The continuity, momentum conservation and energy conservation equations, and corresponding

[a)]Electronic mail: debroy@psu.edu

boundary conditions were transformed into a curvilinear coordinate. The transformed equations were discretized using the control volume method, and then solved using a modified semi-implicit method for pressure linked equations (SIMPLE). The additional heat from the metal droplets was modeled considering the available knowledge base of the interaction between metal droplets and the weld pool. The free surface profile was calculated by minimizing the total free surface energy considering the addition of filler metal. The model was used to quantitatively understand the effect of liquid metal convection on the heat transfer, the role of individual driving forces, and the resulting weld temperature distributions and weld bead geometry.

Due to the complexity of the problem and the clarity of the presentation, the work is divided into two parts: numerical model and application to fillet welding of A-36 mild steel. In this part (part I), the details of the numerical model including coordinate transformation, discretization and solution procedure of governing equations are presented. An application of the model to investigate GMA fillet welding of A-36 steel is presented in part II.

II. ASSUMPTIONS AND SALIENT FEATURES

Because of the complexity of the GMA fillet welding, the following simplifying assumptions were drawn to make the computational work tractable.

(a) Two main thermophysical properties needed for calculations, i.e., the thermal diffusivity and the specific heat of the workpiece material, are assumed to be temperature independent. However, the model is capable of easily incorporating temperature dependent thermophysical properties.

(b) The liquid metal flow is assumed to be incompressible, Newtonian and laminar. The effect of turbulence flow in the weld pool is taken into account through the use of the enhanced thermal conductivity and viscosity of the liquid metal.

(c) The heat transported from the filler metal droplets is taken into account using a time-averaged volumetric heat source.

(d) Both the heat and current flux from the arc are assumed to have Gaussian distribution at the weld top surface. The distribution is unaffected by the top surface deformation.

The heat transfer and fluid flow model takes into account the liquid metal convection in the weld pool, the complex joint geometry of fillet welds, the deformation of the weld pool surface, additions of the filler metal, and the detailed calculations of the heat transfer by the droplets. The driving forces for weld pool convection include the surface tension gradient, electromagnetic force and buoyancy (gravitational) force. The output from the model includes temperature and velocity fields, thermal cycles, fusion zone geometry, and the solidified geometry of the weld reinforcement.

III. HEAT TRANSFER AND FLUID FLOW

A. Governing equations

By using a coordinate system moving with the heat source, the welding problem is assumed to be at steady state. In other words, the heat source is fixed in space and the material enters and leaves the computational domain at the welding speed.[6] Thus, the circulation of liquid metal in the weld pool is represented by the following momentum conservation equation:

$$\rho \frac{\partial (u_i u_j)}{\partial x_i} = \frac{\partial}{\partial x_i}\left(\mu \frac{\partial u_j}{\partial x_i} \right) + S_j , \tag{1}$$

where ρ is the density, x_i is the distance along the ith ($i=1$, 2, and 3) direction, u_i and u_j are the velocity components along the ith and jth direction, respectively, μ is the viscosity, and S_j is the source term for the jth momentum equation and is given as

$$S_j = -\frac{\partial p}{\partial x_j} - \rho U_w \frac{\partial u_j}{\partial x_l} - C\left[\frac{(1-f_l)^2}{f_l^3 + B} \right] u_j + F_j^e + F_j^b , \tag{2}$$

where p represents pressure, U_w is the material moving speed (parallel to the positive x direction, i.e., $i=1$ direction), and F_j^e and F_j^b correspond to the electromagnetic and buoyancy forces, respectively. In Eq. (2), the third term represents the frictional dissipation in the mushy zone according to the Carman–Kozeny equation for flow through a porous media,[18] where f_l is the liquid fraction, B is very small computational constant introduced to avoid division by zero, and C is a constant accounting for the mushy zone morphology.

The following continuity equation is solved in conjunction with the momentum equation to obtain the pressure field:

$$\frac{\partial u_i}{\partial x_i} = 0. \tag{3}$$

By dividing the total enthalpy into the sensible heat and latent heat content,[7,18,19] the energy conservation equation is given as

$$\rho \frac{\partial (u_i h)}{\partial x_i} = \frac{\partial}{\partial x_i}\left(\alpha \frac{\partial h}{\partial x_i} \right) - \rho L \frac{\partial (u_i f_l)}{\partial x_i} - \rho U_w \frac{\partial h}{\partial x_l} - \rho U_w L \frac{\partial f_l}{\partial x_l} + S_v , \tag{4}$$

where h is the sensible heat, α is the thermal diffusion coefficient (defined as $\alpha = k/C_p$, where k is the thermal conductivity and C_p is the specific heat), L is the latent heat of fusion, S_v is a source term accounting for the additional heat from metal droplets. The liquid fraction, f_l, is assumed to vary linearly with temperature

$$f_l = \begin{cases} 1 & T \geqslant T_l \\ \dfrac{T - T_s}{T_l - T_s} & T_s < T < T_l \\ 0 & T \leqslant T_s, \end{cases} \tag{5}$$

where T_l and T_s are the liquidus and solidus temperature of the material, respectively.

B. Coordinate transformation

Accurate solution of heat transfer and fluid flow with a deformable weld pool surface and complex fillet joint geometry requires the use of nonorthogonal deformable grid to

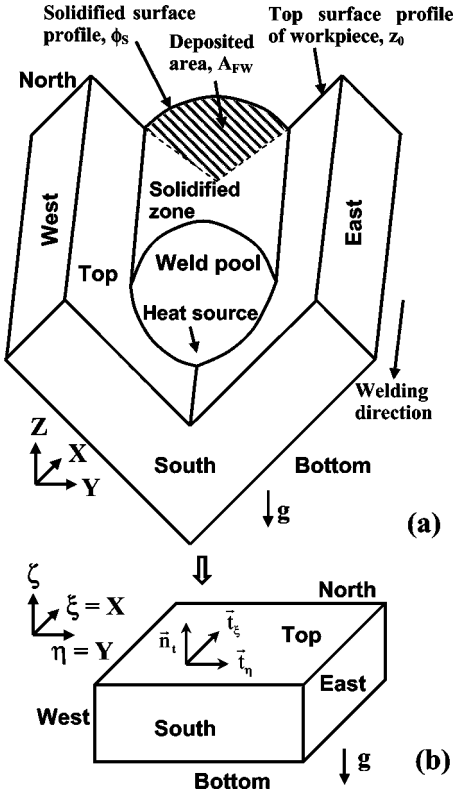

FIG. 1. Schematic plot showing the coordinate transformation from the physical (x,y,z) to the computational domain (ξ,η,ζ): (a) physical domain, and (b) computational domain. Symbols $\mathbf{n}_t$, $\mathbf{t}_\xi$, and $\mathbf{t}_\eta$ are normal and tangential vectors to the top surface. The shadowed area, A_{FW}, is equal to the amount of fed wire per unit length.

exactly fit the curved surface profile. Therefore, the governing equations are transformed from the Cartesian to curvilinear coordinate system. Figure 1 shows the transformation from the L-shape physical domain denoted by (x,y,z) to a simple rectangular computational domain represented by (ξ,η,ζ), where the transformed governing equations were discretized and numerically solved. As shown in this figure, only the z coordinate in the physical domain is transformed into the ζ coordinate in the computational domain, while ξ and η coordinates remain the same as x and y coordinates, respectively. For clarity, subscripts x, y, z, ξ, η and ζ are used to represent corresponding partial derivatives in the following discussion. For example, symbols ξ_x and h_η represent the partial derivatives $\partial\xi/\partial x$ and $\partial h/\partial\eta$, respectively.

The following Chain rule is used for the coordinate transformation:[20,21]

$$\frac{\partial}{\partial x}=\xi_x\frac{\partial}{\partial\xi}+\eta_x\frac{\partial}{\partial\eta}+\zeta_x\frac{\partial}{\partial\zeta},$$

$$\frac{\partial}{\partial y}=\xi_y\frac{\partial}{\partial\xi}+\eta_y\frac{\partial}{\partial\eta}+\zeta_y\frac{\partial}{\partial\zeta}, \tag{6}$$

$$\frac{\partial}{\partial z}=\xi_z\frac{\partial}{\partial\xi}+\eta_z\frac{\partial}{\partial\eta}+\zeta_z\frac{\partial}{\partial\zeta},$$

where the transformation coefficients are expressed as[19]

$$\begin{bmatrix}\xi_x & \xi_y & \xi_z\\ \eta_x & \eta_y & \eta_z\\ \zeta_x & \zeta_y & \zeta_z\end{bmatrix}=\begin{bmatrix}1 & 0 & 0\\ 0 & 1 & 0\\ -Jz_\xi & -Jz_\eta & J\end{bmatrix}, \tag{7}$$

where J is the Jacobian of the transformation and is given as

$$J=\frac{1}{z_\zeta}. \tag{8}$$

The following relationships could be derived from Eqs. (6)–(8):

$$\frac{\partial\phi}{\partial xi}=J\left[\frac{\partial}{\partial\xi}\left(\frac{\xi_{xi}\phi}{J}\right)+\frac{\partial}{\partial\eta}\left(\frac{\eta_{xi}\phi}{J}\right)+\frac{\partial}{\partial\zeta}\left(\frac{\zeta_{xi}\phi}{J}\right)\right], \tag{9}$$

$$\frac{\partial u\phi}{\partial x}+\frac{\partial v\phi}{\partial y}+\frac{\partial w\phi}{\partial z}=J\left[\frac{\partial(U\phi)}{\partial\xi}+\frac{\partial(V\phi)}{\partial\eta}+\frac{\partial(W\phi)}{\partial\zeta}\right], \tag{10}$$

where ϕ is a general variable, xi is the distance along the ith direction ($xi=x$, y, and z when $i=1$, 2, and 3, respectively), u, v, and w are Cartesian velocity components along the x, y, and z directions, respectively, and U, V, and W are the contravariant velocity components in the ξ, η, and ζ directions, respectively, and are defined as

$$U=\frac{\xi_x u}{J}+\frac{\xi_y v}{J}+\frac{\xi_z w}{J}=z_\zeta u,$$

$$V=\frac{\eta_x u}{J}+\frac{\eta_y v}{J}+\frac{\eta_z w}{J}=z_\zeta v, \tag{11}$$

$$W=\frac{\zeta_x u}{J}+\frac{\zeta_y v}{J}+\frac{\zeta_z w}{J}=-z_\xi u-z_\eta v+w.$$

1. Transformation of the continuity equation

Applying Eq. (10), the continuity equation in the curvilinear coordinate is given as

$$\frac{\partial U}{\partial\xi}+\frac{\partial V}{\partial\eta}+\frac{\partial W}{\partial\zeta}=0. \tag{12}$$

2. Transformation of momentum equations

The transformation of x, y, and z momentum equations are very similar. Therefore, in the following discussion, only the transformation of the x momentum equation is given. Using Eqs. (9) and (10), the transformed x momentum equation is given as

$$\begin{aligned}\rho\left[\frac{\partial(Uu)}{\partial\xi}+\frac{\partial(Vu)}{\partial\eta}+\frac{\partial(Wu)}{\partial\zeta}\right]&=\frac{\partial}{\partial\xi}\left[\mu\left(z_\zeta\frac{\partial u}{\partial\xi}-z_\xi\frac{\partial u}{\partial\zeta}\right)\right]\\&+\frac{\partial}{\partial\eta}\left[\mu\left(z_\zeta\frac{\partial u}{\partial\eta}-z_\eta\frac{\partial u}{\partial\zeta}\right)\right]+\frac{\partial}{\partial\zeta}\left[\mu\left(-z_\xi\frac{\partial u}{\partial\xi}\right.\right.\\&\left.\left.-z_\eta\frac{\partial u}{\partial\eta}+q_{33}\frac{\partial u}{\partial\zeta}\right)\right]-\left(z_\zeta\frac{\partial p}{\partial\xi}-z_\xi\frac{\partial p}{\partial\zeta}\right)\\&-\rho U_w\left[\frac{\partial(z_\zeta u)}{\partial\xi}-\frac{\partial(z_\xi u)}{\partial\zeta}\right]-C\left[\frac{(1-f_l)^2}{f_l^3+B}\right]z_\zeta u+z_\zeta F_x^e\\&+z_\zeta F_x^b,\end{aligned} \tag{13}$$

where coefficient q_{33} is defined as

$$q_{33}=J(z_\xi^2+z_\eta^2+1). \tag{14}$$

3. Transformation of energy conservation equation

The transformed energy equation in the curvilinear coordinate system is given as

$$\rho\left[\frac{\partial(Uh)}{\partial\xi}+\frac{\partial(Vh)}{\partial\eta}+\frac{\partial(Wh)}{\partial\zeta}\right]=\frac{\partial}{\partial\xi}\left[\alpha\left(z_\zeta\frac{\partial h}{\partial\xi}-z_\xi\frac{\partial h}{\partial\zeta}\right)\right]+\frac{\partial}{\partial\eta}\left[\alpha\left(z_\zeta\frac{\partial h}{\partial\eta}-z_\eta\frac{\partial h}{\partial\zeta}\right)\right]+\frac{\partial}{\partial\zeta}\left[\alpha\left(-z_\xi\frac{\partial h}{\partial\xi}-z_\eta\frac{\partial h}{\partial\eta}+q_{33}\frac{\partial h}{\partial\zeta}\right)\right]-\rho U_w\left[\frac{\partial(z_\zeta h)}{\partial\xi}-\frac{\partial(z_\xi h)}{\partial\zeta}\right]-\rho L\left[\frac{\partial(Uf_l)}{\partial\xi}+\frac{\partial(Vf_l)}{\partial\eta}+\frac{\partial(Wf_l)}{\partial\zeta}\right]-\rho U_w L\left[\frac{\partial(z_\zeta f_l)}{\partial\xi}-\frac{\partial(z_\xi f_l)}{\partial\zeta}\right]+z_\zeta S_v. \tag{15}$$

C. Driving forces for liquid convection and boundary conditions

1. Driving forces

The driving forces for the liquid metal convection considered in the present study are the electromagnetic force, buoyancy force, and shear stress due to the surface tension gradient at the weld pool top surface. The electromagnetic force, $\mathbf{F}^e$, is given as

$$\mathbf{F}^e=\mathbf{J}\times\mathbf{B}, \tag{16}$$

where $\mathbf{J}$ and $\mathbf{B}$ are the current flux and magnetic field in the workpiece, respectively. In this study, the electromagnetic force is approximated using equations derived for a rectangular domain[22] to simplify the calculation.

Using the Boussinesq approximation, the buoyancy force, $\mathbf{F}^b$, is given as

$$\mathbf{F}^b=-\rho\mathbf{g}\beta(T-T_{\text{ref}}),$$

where $\mathbf{g}$ is the gravity acceleration and is in the negative z or ζ direction, β is the thermal expansion coefficient, T and T_{ref} are the local and arbitrarily selected reference temperatures, respectively.

The third driving force for the weld pool convection, i.e., the Marangoni sheer stress due to the surface tension gradient, is discussed in the boundary conditions for momentum equations.

2. Boundary conditions for momentum equations

The velocities at the weld pool top surface are given as

$$\mathbf{v}\cdot\mathbf{n}_t=0, \tag{17a}$$

$$\mu\nabla(\mathbf{v}\cdot\mathbf{t}_\xi)\cdot\mathbf{n_t}=f_l\left(\frac{d\gamma}{dT}\right)\nabla T\cdot\mathbf{t}_\xi, \tag{17b}$$

$$\mu\nabla(\mathbf{v}\cdot\mathbf{t}_\eta)\cdot\mathbf{n_t}=f_l\left(\frac{d\gamma}{dT}\right)\nabla T\cdot\mathbf{t}_\eta, \tag{17c}$$

where $\mathbf{v}$ is the liquid metal velocity, $d\gamma/dT$ is the temperature coefficient of surface tension, $\mathbf{n}_t$ is the local unit normal vector to the top surface, and $\mathbf{t}_\xi$ and $\mathbf{t}_\eta$ are local unit tangential vectors to the top surface along the ξ and η directions, respectively. Equation (17a) indicates that the normal velocity to the weld pool top surface is zero, while Eqs. (17b) and (17c) represent the Marangoni sheer stress at the top surface. As shown in Fig. 1(b), the normal and tangential vectors to the weld pool top surface are given as

$$\mathbf{n}_t=\frac{\zeta_x\mathbf{i}+\zeta_y\mathbf{j}+\zeta_z\mathbf{k}}{\sqrt{\zeta_x^2+\zeta_y^2+\zeta_z^2}},\quad \mathbf{t}_\xi=\frac{x_\xi\mathbf{i}+y_\xi\mathbf{j}+z_\xi\mathbf{k}}{\sqrt{x_\xi^2+y_\xi^2+z_\xi^2}},$$

$$\mathbf{t}_\eta=\frac{x_\eta\mathbf{i}+y_\eta\mathbf{j}+z_\eta\mathbf{k}}{\sqrt{x_\eta^2+y_\eta^2+z_\eta^2}}, \tag{18}$$

where $\mathbf{i}$, $\mathbf{j}$, and $\mathbf{k}$ are the unit vectors along x, y, and z directions, respectively.

The liquid metal velocity at all other surfaces, i.e., bottom, east, west, south, and north surfaces, are equal to zero.

3. Boundary conditions for energy conservation equation

The boundary conditions for energy conservation equation are the same as those published in our previous article.[19] Therefore, only salient features are described later.

As shown in Fig. 1(a), the heat flux at the top surface, F_t, is given as

$$\alpha\nabla h\cdot\mathbf{n}_t=F_t=\frac{IV\eta}{2\pi r_b^2}\exp\left(-\frac{x_h^2+y_h^2}{2r_b^2}\right)(\mathbf{k}\cdot\mathbf{n}_t)-\sigma\epsilon(T^4-T_a^4)-h_c(T-T_a), \tag{19}$$

where I is the current, V is the voltage, η is the arc efficiency, r_b is the heat distribution parameter, x_h and y_h are the x and y distances to the arc axis, respectively, σ is the Stefan–Boltzmann constant, ϵ is the emissivity, h_c is the convective heat transfer coefficient, and T_a is the ambient temperature.

For the bottom surface, the heat flux, F_b, is given as

$$\alpha\nabla h\cdot\mathbf{n}_b=F_b=h_c(T-T_a), \tag{20}$$

where $\mathbf{n}_b$ is a unit normal vector to the bottom surface. The temperatures at other surfaces, i.e., east, west, south, and north surfaces are set to the ambient temperature.

D. Grid system and discretization of the governing equations

The governing equations are discretized using the control volume method, where the computational domain is divided into small rectangular control volumes, as shown in Fig. 2. A scalar grid point is located at the center of each control volume, storing the values of scalar quantities such as pressure and enthalpy. Velocity components lie at the control volume faces, staggered with respect to scalar locations. For example, both Cartesian v velocity and contravariant V velocity are placed at the south and north faces of a control volume P, as shown in Fig. 2. Thus, the control volumes for

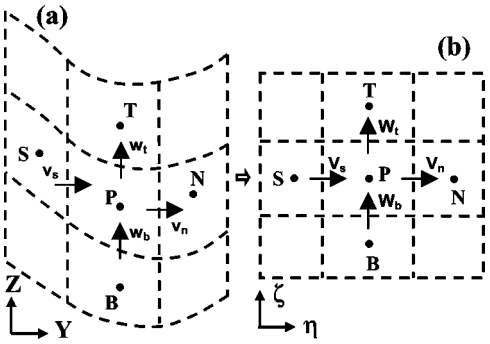

FIG. 2. Grid system in the physical and computational domains: (a) a *YZ* plane in the physical domain, and (b) the corresponding $\eta\zeta$ plane in the computational domain. Dashed lines represent control volume's interfaces, while solid dots indicate scalar grid points. Symbols *W, E, S, N, B, T* are the east, west, south, north, bottom, and top neighbors of the grid point *P*, respectively, while symbols *s, n, b, t* are the south, north, bottom, and top interfaces of the control volume *P*.

vectors are different from those for scalars. Such an arrangement is extensively used in orthogonal coordinates preventing unrealistic solution of velocity and pressure fields.[23] Discretized equations for a variable are formulated by integrating the corresponding governing equation over the control volumes in the computational domain. A power-law based scheme is used to describe the convective flux at the control volume faces. The final expression can be written in the following general form as:[23]

$$a_P\phi_P = a_E\phi_E + a_W\phi_W + a_N\phi_N + a_S\phi_S + a_T\phi_T + a_B\phi_B + b, \tag{21}$$

where a_E, a_W, etc., denote the combined convection-diffusion coefficients and b includes all the source terms.

E. Modified SIMPLE algorithm for the calculation of velocity field

The governing equations, i.e., continuity, momentum, and energy conservation equations, need to be solved "simultaneously" to obtain temperature and velocity fields. A modified SIMPLE algorithm[23] is used to solve the discretized equations. The modification takes into account the main feature in the transformed governing equations in the curvilinear coordinate system, i.e., a mixed Cartesian-contravariant velocity components.

1. Discretized momentum equations

As discussed in the previous section, the discretize momentum equations are obtained by integrating the momentum equations over the corresponding control volumes. Figure 3 shows a control volume for the v velocity which is staggered in the η direction. The discretized equation for v_n can be seen to be

$$a_n^v v_n = \sum a_{nb} v_{nb} + b + A_n z_\zeta (p_P - p_N), \tag{22}$$

where subscripts *n, p, P, N*, etc., indicate the location where a variable is evaluated, and A_n is the area of the north face. Similar equations for Cartesian velocity components *u* and *w* can be written.

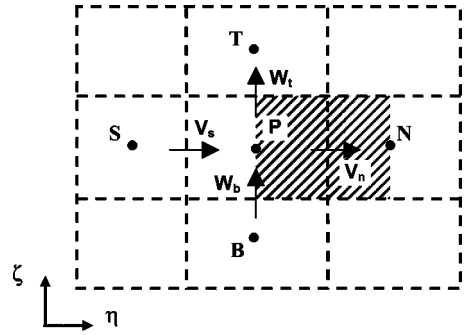

FIG. 3. Control volume for v or V velocity component in the computational domain. For clarity, only the $\eta\zeta$ section is shown.

2. Pressure and velocity corrections

Suppose the velocity field at an intermediate step of the iterative solution procedure is given by u^*, v^*, and w^*, corresponding to a guessed pressure field p^*. For example, the "starred" v velocity field results from the solution of the following discretized v momentum equation

$$a_n^v v_n^* = \sum a_{nb}^v v_{nb}^* + b + A_n z_\zeta (p_P^* - p_N^*). \tag{23}$$

The correct pressure and velocity fields can be obtained from

$$p = p^* + p'; \quad u = u^* + u'; \quad v = v^* + v'; \quad w = w^* + w', \tag{24}$$

where p', u', v', and w' are corresponding corrections.

Subtract Eq. (23) from Eq. (22), we have

$$a_n^v v_n' = \sum a_{nb}^v v_{nb}' + A_n z_\zeta (p_P' - p_N'). \tag{25}$$

Ignoring the first term on the right-hand side of Eq. (25), the following v velocity-correction formula is obtained

$$v_n' = \frac{A_n z_\zeta (p_P' - p_N')}{a_n^v}. \tag{26}$$

Similarly, the *u* and *w* velocity-correction formulas are given as

$$u_e' = \frac{A_e z_\zeta (p_P' - p_E')}{a_e^u}, \tag{27}$$

$$w_t' = \frac{A_t (p_P' - p_T')}{a_t^w}. \tag{28}$$

3. Continuity equation

Substituting Eq. (11) into Eq. (3), the continuity equation in the curvilinear coordinate can be rewritten as

$$\frac{\partial (z_\zeta u)}{\partial \xi} + \frac{\partial (z_\zeta v)}{\partial \eta} + \frac{\partial (w - z_\xi u - z_\eta v)}{\partial \zeta} = 0. \tag{29}$$

Integrating the earlier equation over the scalar control volume *P* shown in Fig. 3, the discretized continuity equation is given as

$$A_e[(z_\zeta u)_e-(z_\zeta u)_w]+A_n[(z_\zeta v)_n-(z_\zeta v)_s]+A_t[w_t-w_b]$$
$$=A_t[(z_\xi u+z_\eta v)_t-(z_\xi u+z_\eta v)_b]. \quad (30)$$

If we now substitute for all the velocity components the expressions given by the velocity-correction formulas, we obtain, after rearrangement, the following discretization equation for p′:

$$a_P p'_P=a_E p'_E+a_W p'_W+a_N p'_N+a_S p'_S+a_T p'_T+a_B p'_B+b_p, \quad (31)$$

where

$$a_E=\frac{A_e^2(z_\zeta)_e^2}{a_e^u}, \quad (32a)$$

$$a_W=\frac{A_e^2(z_\zeta)_w^2}{a_w^u}, \quad (32b)$$

$$a_N=\frac{A_n^2(z_\zeta)_n^2}{a_n^v}, \quad (32c)$$

$$a_S=\frac{A_n^2(z_\zeta)_s^2}{a_s^v}, \quad (32d)$$

$$a_T=\frac{A_t^2}{a_t^w}, \quad (32e)$$

$$a_B=\frac{A_t^2}{a_b^w}, \quad (32f)$$

$$a_P=a_E+a_W+a_N+a_S+a_T+a_B, \quad (32g)$$

$$b_p=A_e(U_w^*-U_e^*)+A_n(V_s^*+V_n^*)+A_t(W_b^*-W_t^*). \quad (32h)$$

4. Modified SIMPLE algorithm

The modified SIMPLE algorithm is listed later.

(1) Guess the pressure field p^*.
(2) Solve the discretized momentum equations, such as Eq. (22), to obtain u^*, v^*, and w^*. Then, the corresponding contravariant velocity is updated using Eq. (11).
(3) Solve the p' equation, i.e., Eq. (31).
(4) Calculate p using Eq. (24) by adding p' to p^*.
(5) Calculate u, v, w from their starred values using the velocity-correction formulas (26)–(28). Then, update contravariant velocity components using Eq. (11).
(6) Solve the discretized energy equation using the latest values of contravariant velocities.
(7) Update the solution domain for the momentum equations and material properties based on the current temperature field.
(8) Treat the corrected pressure p as a new guessed pressure p^*, return to step 2, and repeat the whole procedure until a converged solution is obtained.

IV. HEAT TRANSFER FROM METAL DROPLETS

Molten droplet transfer is one of the characteristics of GMA welding, and it makes the welding process highly productive. There are three basic modes of transferring the molten metal at the fed wire tip to the weld pool: globular, spray, and short-circuiting.[2,24] Spray transfer mode is often observed at medium and high currents. In this mode, small discrete metal drops travel across the arc gap at high frequency and speed, which enables highly stable metal transfer and less spatters. For GMA welding of thick workpiece, spray transfer mode is often preferred for its stability and efficiency.

An important feature of the GMA weld bead is the finger penetration mainly caused by the transfer of heat from the superheated metal droplets into the weld pool. For the spray transfer mode, previous research work in butt[25,26] and fillet welding[19] has shown that the droplet heat transfer can be effectively simulated by incorporating a time-averaged volumetric heat source term (S_v) in the energy conservation equation. This approach is also employed here, since the welding conditions studied are consistent with those for spray transfer mode.

A. Calculation of volumetric heat source

The volumetric heat source is characterized by its radius (R_v), height (d), and power density (S_v). In our previous study, we have developed a procedure to calculate these parameters by considering the available knowledge base of the interaction between metal droplets and weld pool for various welding conditions.[19] Salient features are summarized as follows.

The radius of the volumetric heat source is assumed to be twice as the droplet radius, and the height (d) is calculated from the following equation based on energy balance:[2,25]

$$d=h_v-x_v+D_d, \quad (33)$$

where h_v is the estimated height of cavity by the impact of metal droplets, x_v is the distance traveled by the center of the slug between the impingement of two successive droplets, and D_d is the droplet diameter.

The total sensible heat input from the metal droplets, Q_t, is given as

$$Q_t=\rho\pi r_w^2 w_f H_d, \quad (34)$$

where ρ is the density, r_w is the radius of the wire, w_f is the wire feeding rate, and H_d is the total enthalpy of the droplets. It should be noted that a portion of Q_t is used to heat the additional metal from the droplets up to liquidus temperature. Therefore, the effective heat of droplets (Q_d) carrying into the weld pool is given as[16]

$$Q_d=\rho\pi r_w^2 w_f C_{\mathrm{pl}}(T_d-T_l), \quad (35)$$

where C_{pl} is the specific heat of the liquid metal, T_d is the droplet temperature and is assumed to be 2673 K,[27] and T_l is the liquidus temperature.

The values of h_v and x_v in Eq. (33) are calculated based on energy balance as[2,25]

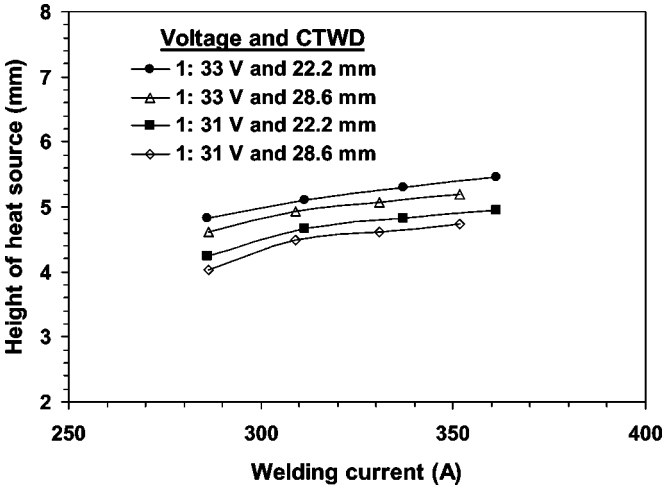

FIG. 4. Calculated height of the volumetric heat source for various welding conditions. Symbol CTWD represents the contact tube to workpiece distance.

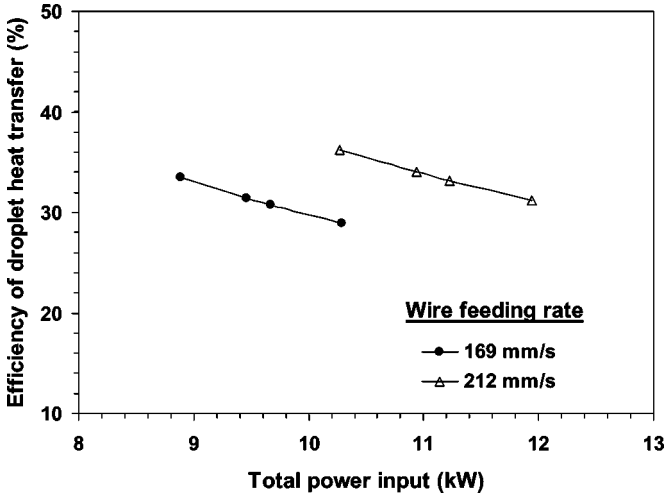

FIG. 5. Calculated efficiency of droplet heat transfer. The efficiency of droplet heat transfer is defined as the ratio of the total sensible heat input from metal droplets over the total power input.

$$h_v = \left\{ -\frac{2\gamma}{D_d \rho g} + \sqrt{\left[\left(\frac{2\gamma}{D_d \rho g} \right)^2 + \frac{D_d v_d^2}{6g} \right]} \right\} \tag{36}$$

$$x_v = \left(h_v + \frac{2\gamma}{D_d \rho g} \right) \left\{ 1 - \cos\left[\left(\frac{g}{h_v} \right)^{1/2} \Delta t \right] \right\}, \tag{37}$$

where γ is the surface tension of the molten metal ($\mathrm{N\,m^{-1}}$), g is the gravitational constant, v_d is the droplet impingement velocity, and Δt is the interval between two successive drops ($\Delta t = 1/f$, where f is the droplet transfer frequency). As shown in Eqs. (33)–(37), calculation of the dimensions of the volumetric heat source requires the knowledge of the droplet transfer frequency, radius, and impingement velocity. These parameters are determined from the knowledge base available in the literature for given welding conditions. The calculation procedure is available in Ref. 19. From the computed values of Q_d, D_d, and d, the time-averaged power density of the volumetric heat source, S_v, is calculated as follows:

$$S_v = \frac{Q_d}{\pi D_d^2 d}. \tag{38}$$

It should be noted that S_v only applies for grid points within the cylindrical heat source, and the power density is zero outside the cylinder.

B. Effect of welding parameters on volumetric heat source

The effects of current, voltage, and contact tube to workpiece distance (CTWD) on the computed height of the volumetric heat source are shown in Fig. 4. As shown in this figure, it is found that the height of the heat source rises with both welding current and voltage, while it drops with the increase in CTWD. The influence of current can be understood from its effect on the droplet impingement velocity, which increases with current. The higher velocity, in turn, increases the height of the heat source, as can be observed from Eq. (36). When the voltage is increased keeping the current constant, both the arc length and the droplet impingement velocity increase. As a result, the height of the volumetric heat source also increases with voltage. With the increase in CTWD the impingement velocity decreases which leads to a reduction of the height of the heat source. This is because the increase in CTWD is accompanied by an increase in the wire feeding rate to maintain a target current. As a consequence, the droplet radius increases and the impingement velocity decreases. It will be shown in the next paragraph that the droplets carry a significant amount of energy into the weld pool for the welding conditions investigated. Under these conditions, the height of the volumetric heat source significantly affects finger penetration which is a characteristic of GMA welds.

Figure 5 shows the efficiency of droplet heat transfer (η_d), defined as the ratio of the total sensible heat input owing to metal droplets (Q_t) over the total heat input (IV), i.e., $\eta_d = Q_t/(IV)$. Since the droplet temperature does not change significantly for the welding conditions used in this study,[27] the droplet heat transfer rate is determined by the wire feeding rate. Therefore, at a given wire feeding rate, the efficiency of droplet heat transfer is inversely proportional to the total heat input, as shown in Fig. 5. On the other hand, the higher the wire feeding rate, the higher the droplet heat transfer efficiency for the same amount of total power input, as evident from Eq. (35). The computed values of the efficiency of droplet heat transfer are found to vary between 28% and 36% for all the cases studied here, which is consistent with the 25%±5% value reported in Essers and Walters' experimental measurements for similar welding conditions.[28] The entire sensible heat of the droplets is distributed to a small cylindrical volume directly under the arc and this distribution of heat is the main reason for the finger penetration observed in the fusion zone of GMA fillet welds.

V. WELD POOL TOP SURFACE PROFILE

At high current, the weld pool surface becomes significantly depressed under the action of arc pressure.[29,30] In

GMA welding, the addition of filler metal by means of metal transfer further displaces the weld pool surface. Therefore, the assumption of a flat pool surface is no longer valid. A numerical model needs to take into account the depressed surface profile to correctly and accurately calculate the heat transfer and fluid flow during GMA fillet welding.

A. Minimization of total surface energy

At steady state, the top surface profile of the liquid weld pool can be determined using the energy minimization method. The total energy to be minimized includes the surface energy due to the change in area of the pool surface, the potential energy in the gravitational field and the work performed by the arc pressure displacing the pool surface. Detailed procedure for the calculation of the free surface profile is available in the literature,[19] and only salient features are presented here.

The following two equations are solved to obtain the weld pool surface profile:

$$\gamma\left[\frac{(1+\phi_y^2)\phi_{xx}-2\phi_x\phi_y\phi_{xy}+(1+\phi_x^2)\phi_{yy}}{(1+\phi_x^2+\phi_y^2)^{3/2}}\right]=\rho g\phi+P_a+\lambda, \tag{39}$$

$$\int (\phi_s-z_0)dy-\frac{\pi r_w^2 w_f}{U_w}=0. \tag{40}$$

In Eq. (39), subscripts x and y represent partial derivative with respect to x and y, respectively, γ is the surface tension, P_a is the arc pressure distribution at the pool top surface (discussed in the next section), and λ is the Lagrange multiplier. In Eq. (40), r_w, w_f, and U_w are the wire radius, wire feeding rate, and the welding speed, respectively, and ϕ_s is the solidified surface profile, z_0 is the z location of the workpiece top surface, as shown in Fig. 1. Equation (39) represents the static force balance at the pool top surface, while Eq. (40) defines a constraint condition that the deposited area, A_{FW}, at a solidified cross section of the fillet weld is equal to the amount of fed wire per unit length, as shown in Fig. 1.

The boundary conditions for the free surface equation are given as

$$\text{At the front pool boundary: } \phi=z_0, \tag{41a}$$

$$\text{At the rear pool boundary: } \frac{\partial\phi}{\partial x}=0, \tag{41b}$$

where the front and rear pool boundaries are defined so that the temperature gradient along the x direction (dT/dx) is positive at the front pool boundary and negative at the rear boundary.

To obtain the free surface profile, both Eqs. (39) and (40) need to be solved. Equation (39) is discretized using the finite difference method. It is then solved using the Gauss–Seidel point-by-point method[23] for an assumed λ with appropriate boundary conditions. The resulting free surface profile is applied to the constraint Eq. (40), and the residual [defined as the left-hand side of Eq. (40)] is evaluated. The value of λ is determined iteratively using the bisection method[31] until both Eqs. (39) and (40) are satisfied.

B. Arc pressure distribution

The arc pressure P_a is normally approximated by a Gaussian distribution as:[29,30]

$$P_a=\frac{F}{2\pi\sigma_P^2}\exp\left(-\frac{x_h^2+y_h^2}{2\sigma_p^2}\right), \tag{42}$$

where F is the total arc force, σ_p is the distribution parameter for arc pressure, and x_h and y_h are the x and y distances to the arc axis, respectively. As shown in Eq. (42), the calculation of arc pressure distribution at the weld pool top surface requires the knowledge of the total force and the distribution parameter. Lin and Eagar experimentally measured the arc pressure distribution for tungsten electrodes with three different electrode tip angles, 30°, 60°, and 90°.[29] Their measurements indicated that both F and σ_P depended strongly on the welding current. Therefore, in this study, the relationship of F and σ_P as a function of current was extracted from their experimental data[29] for three tip angles. For instance, the total arc force was calculated by integrating the measured arc pressure distribution data

$$F=\int 2\pi r P_a' dr, \tag{43}$$

where P_a' is the measured arc pressure at a distance of r from the arc axis. Once the total arc force was obtained, the pressure distribution parameter was then determined by fitting the experimental distribution into the Eq. (42).

The calculated total arc force and pressure distribution parameter as a function of current, I, are given in the following equations:

$$F=\begin{cases}-0.060\,49+0.000\,280\,8\times I(\mathrm{N}) & (30^\circ \text{ tip angle})\\ -0.040\,17+0.000\,255\,3\times I(\mathrm{N}) & (60^\circ \text{ tip angle})\\ -0.043\,07+0.000\,198\,1\times I(\mathrm{N}) & (90^\circ \text{ tip angle})\end{cases}, \tag{44}$$

$$\sigma_{\mathrm{P}}=\begin{cases}0.7725+0.001\,93\times I(\mathrm{mm}) & (30^\circ \text{ tip angle})\\ 1.4875+0.001\,23\times I(\mathrm{mm}) & (60^\circ \text{ tip angle})\\ 1.4043+0.001\,74\times I(\mathrm{mm}) & (90^\circ \text{ tip angle})\end{cases}, \tag{45}$$

where I is current in ampere. These relationships were also plotted graphically in Figs. 6 and 7. As shown in these figures, sharp electrode tip results in a concentrated arc pressure distribution for a given current. Both total arc force and pressure distribution parameters increase with current. In the present calculation, the calculated σ_P for 60° tip angle was used, while F was taken as the average of those for three tip angles, shown in following equations:

$$F=-0.047\,91+0.00\,0244\,7\times I(\mathrm{N}), \tag{46}$$

$$\sigma_P=1.4875+0.001\,23\times I(\mathrm{mm}). \tag{47}$$

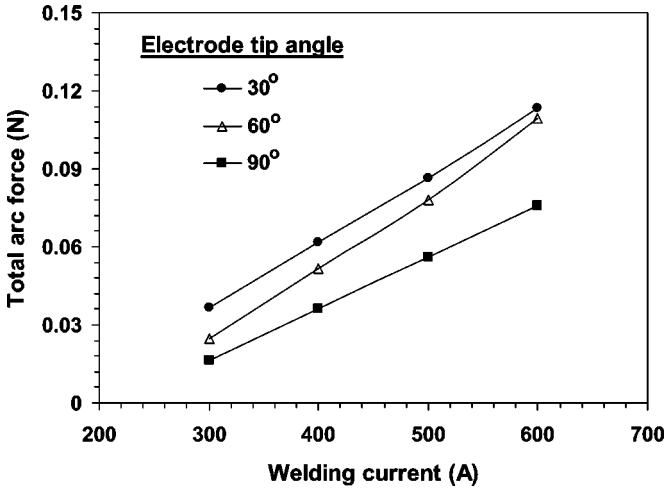

FIG. 6. Calculated total arc force as a function of current for three different tip angles.

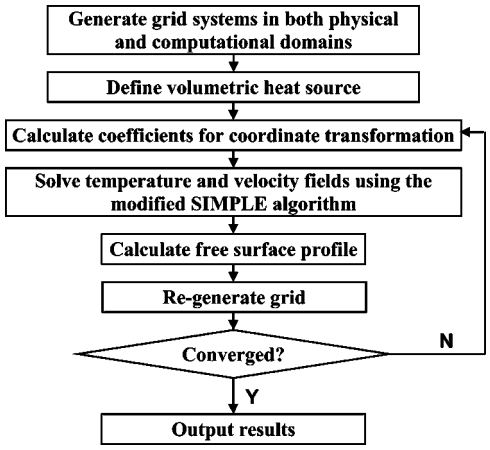

FIG. 8. Schematic diagram showing the overall iterative procedure for the calculation of temperature and velocity fields and surface profile during GMA fillet welding.

VI. OVERALL SOLUTION PROCEDURE

The governing equations are solved ''simultaneously'' to obtain the temperature and velocity fields and the free surface profile. Figure 8 is a flow chart showing the overall iterative procedure used in the heat transfer and fluid flow model. First, the modified SIMPLE algorithm is used to calculate the temperature and velocity fields. Then, the free surface profile is calculated based on the temperature field obtained in the previous step. After the solution of the free surface profile, the z locations of grids are adjusted to fit the surface profile, and the temperature and velocity fields are then recalculated in the fitted grid system. The calculation procedure is repeated until converged temperature and velocity fields and free surface profile are obtained.

A $72\times66\times47$ grid system was used and the corresponding solution domain had dimensions of 450 mm in length, 108 mm in width, and 18 mm in depth. Spatially nonuniform grids with finer grids near the heat source were used for maximum resolution of variables. The calculations normally converged within 5000 iterations, which took about 30 min in a PC with 2.8 GHz Intel P4 CPU and 512 Mb PC2700 DDR-SDRAM memory. Comparing with the heat transfer model[19] which converges in 4000 iterations (about 6 min), the heat transfer and fluid flow calculation is much more computationally intensive.

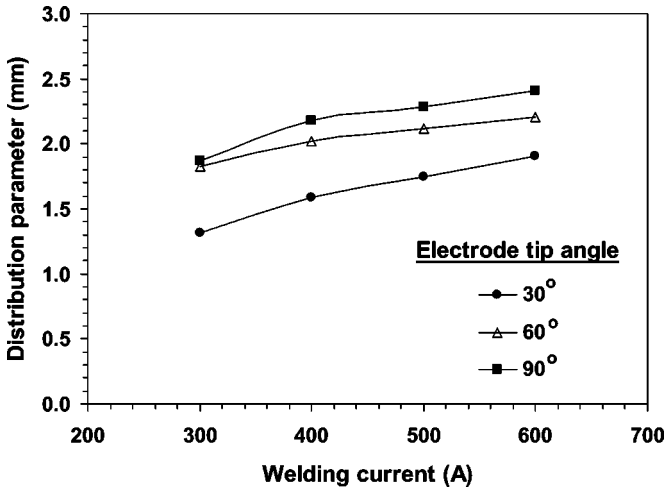

FIG. 7. Calculated arc pressure distribution parameter as a function of current for three different tip angles.

VII. SUMMARY AND CONCLUSIONS

A three-dimensional numerical heat transfer and fluid flow model was developed to calculate the temperature profiles, velocity field, weld pool shape and size, and the nature of the solidified weld pool reinforcement surface during GMA welding of fillet joints. The present part (part I) is focused on the details of the numerical heat transfer and fluid flow model, which has the following salient features.

(1) The numerical model solves the continuity, momentum conservation and energy conservation equations in a boundary fitted coordinate system. The governing conservation equations and the corresponding boundary conditions were transformed into the curvilinear coordinate system and then discretized in a simple rectangular computational domain. A modified SIMPLE algorithm was used to simultaneously solve the discretized equations to obtain the temperature and velocity fields.

(2) The driving forces for liquid metal convection in the weld pool include surface tension, buoyancy and electromagnetic forces.

(3) The heat transfer from metal droplets was simulated using a volumetric heat source. A procedure was established to calculate the radius, height and power density of the volumetric heat source based on the experimental data for GMA welding available in the literature.

(4) The weld pool surface profile was calculated by minimizing the total surface energy, which includes the surface tension energy, gravity potential, and work done by arc force.

In part II of this work, an application of this model to GMA fillet welding of A-36 mild steel is described.

ACKNOWLEDGMENTS

The work was supported by a grant from the U.S. Department of Energy, Office of Basic Energy Sciences, Division of Materials Sciences, under Grant No. DE-FGO2-01ER45900. W. Z. gratefully acknowledges the award of a Fellowship from the American Welding Society. Valuable critical comments from Dr. A. De, Y. Fan, X. He, A. Kumar, and S. Mishra are appreciated.

[1] S. A. David and T. DebRoy, Science **257**, 497 (1992).
[2] J. F. Lancaster, *The Physics of Welding*, 2nd ed. (Pergamon, Oxford, 1986).
[3] T. DebRoy and S. A. David, Rev. Mod. Phys. **67**, 85 (1995).
[4] M. C. Tsai and S. Kou, Weld. J. (Miami, FL, U. S.) **69**, 241s (1990).
[5] X. He, P. W. Fuerschbach, and T. DebRoy, J. Phys. D **36**, 1388 (2003).
[6] K. Mundra, T. DebRoy, and K. M. Kelkar, Numer. Heat Transfer, Part A **29**, 115 (1996).
[7] W. Zhang, G. G. Roy, J. W. Elmer, and T. DebRoy, J. Appl. Phys. **93**, 3022 (2003).
[8] W. Zhang, J. W. Elmer, and T. DebRoy, Mater. Sci. Eng., A **333**, 320 (2002).
[9] J. W. Elmer, T. A. Palmer, W. Zhang, B. Wood, and T. DebRoy, Acta Mater. **51**, 3333 (2003).
[10] Z. Yang, J. W. Elmer, J. Wong, and T. DebRoy, Weld. J. (Miami, FL, U. S.) **79**, 97s (2000).
[11] Z. Yang, S. Sista, J. W. Elmer, and T. DebRoy, Acta Mater. **48**, 4813 (2000).
[12] T. Hong, W. Pitscheneder, and T. DebRoy, Sci. Technol. Weld. Joining **3**, 33 (1998).
[13] K. Mundra, J. M. Blackburn, and T. DebRoy, Sci. Technol. Weld. Joining **2**, 174 (1997).
[14] C. S. Wu and L. Dorn, Comput. Mater. Sci. **2**, 341 (1994).
[15] J.-W. Kim and S.-J. Na, Weld. J. (Miami, FL, U. S.) **74**, 141s (1995).
[16] Z. N. Cao and P. Dong, J. Eng. Mater. Technol. **120**, 313 (1998).
[17] H. G. Fan and R. Kovacevic, J. Phys. D **31**, 2929 (1998).
[18] V. R. Voller and C. Prakash, Int. J. Heat Mass Transfer **30**, 1709 (1987).
[19] C.-H. Kim, W. Zhang, and T. DebRoy, J. Appl. Phys. **94**, 2667 (2003).
[20] K. A. Hoffmann and S. T. Chiang, *Computational Fluid Dynamics for Engineering—Volume II* (Engineering Education System, Wichita, KS, 1993).
[21] J. F. Thompson, Z. U. A. Warsi, and C. Wayne Mastin, *Numerical Grid Generation: Fundamentals and Applications* (Elsevier Science, New York, 1985).
[22] S. Kou and Y. H. Wang, Metall. Trans. A **17A**, 2271 (1986).
[23] S. V. Patankar, *Numerical Heat Transfer and Fluid Flow* (McGraw-Hill, New York, 1982).
[24] S. Kou, *Welding Metallurgy*, 2nd ed. (Wiley, Hoboken, New Jersey, 2003).
[25] S. Kumar and S. C. Bhaduri, Metall. Mater. Trans. B **25B**, 435 (1994).
[26] Z. Yang and T. DebRoy, Metall. Mater. Trans. B **30B**, 483 (1999).
[27] G. Jelmorini, G. W. Tichelaar, and G. J. P. M. Van den Heuvel, *IIW Document 212-411-77* (International Institute of Welding, London, 1977).
[28] W. G. Essers and R. Walter, Weld. J. (Miami, FL, U. S.) **60**, 37s (1981).
[29] M. L. Lin and T. W. Eagar, Metall. Trans. B **17B**, 601 (1986).
[30] Y. S. Kim and T. W. Eagar, Weld. J. (Miami, FL, U. S.) **70**, 20s (1991).
[31] W. H. Press, B. P. Flannery, S. A. Teukolsky, and W. T. Vetterling, *Numerical Recipes in* FORTRAN, 2nd ed. (Cambridge University Press, Cambridge, 1992).